Electrochemical Activation of Atomic Layer-Deposited Cobalt Phosphate Electrocatalysts for Water Oxidation

Ruoyu Zhang,[§] Gerben van Straaten,[§] Valerio di Palma, Georgios Zafeiropoulos, Mauritius C.M. van de Sanden, Wilhelmus M.M. Kessels, Mihalis N. Tsampas,* and Mariadriana Creatore*

Read Online

ACCESS | Metrics & More | Article Recommendations | SI Supporting Information

ABSTRACT: The development of efficient and stable earth-abundant water oxidation catalysts is vital for economically feasible water-splitting systems. Cobalt phosphate (CoPi)-based catalysts belong to the relevant class of nonprecious electrocatalysts studied for the oxygen evolution reaction (OER). In this work, an in-depth investigation of the electrochemical activation of CoPi-based electrocatalysts by cyclic voltammetry (CV) is presented. Atomic layer deposition (ALD) is adopted because it enables the synthesis of CoPi films with cobalt-to-phosphorous ratios between 1.4 and 1.9. It is shown that the pristine chemical composition of the CoPi film strongly influences its OER activity in the early stages of the activation process as well as after prolonged exposure to the electrolyte. The best performing CoPi catalyst, displaying a current density of 3.9 mA cm^{-2} at 1.8 V versus reversible hydrogen electrode and a Tafel slope of 155 mV/dec at pH 8.0, is selected for an in-depth study of the evolution of its electrochemical properties, chemical composition, and electrochemical active surface area (ECSA) during the activation process. Upon the increase of the number of CV cycles, the OER performance increases, in parallel with the development of a noncatalytic wave in the CV scan, which points out to the reversible oxidation of Co^{2+} species to Co^{3+} species. X-ray photoelectron spectroscopy and Rutherford backscattering measurements indicate that phosphorous progressively leaches out the CoPi film bulk upon prolonged exposure to the electrolyte. In parallel, the ECSA of the films increases by up to a factor of 40, depending on the initial stoichiometry. The ECSA of the activated CoPi films shows a universal linear correlation with the OER activity for the whole range of CoPi chemical composition. It can be concluded that the adoption of ALD in CoPi-based electrocatalysis enables, next to the well-established control over film growth and properties, to disclose the mechanisms behind the CoPi electrocatalyst activation.

KEYWORDS: cobalt phosphate, atomic layer deposition, oxygen evolution reaction, electrochemical activation, catalyst restructuring

INTRODUCTION

Meeting the word's energy requirements by adopting renewable sources, such as wind and solar energy, also demands viable solutions in terms of electricity storage.[1] A valid approach is water electrolysis, yielding hydrogen and oxygen, which can then be converted back to electricity on-demand[2] or serve as building blocks for the production of synthetic fuels.[3] However, the energy efficiency of the water electrolysis process currently employed in the industry is limited by the sluggish kinetics and high overpotentials of the oxygen evolution reaction (OER).[4] State-of-the-art catalysts for the OER with much higher activities and lower overpotentials than those used in industries are available, but they are made of noble metal oxides.[1] Although these catalysts lead to high energy efficiencies, the resources they are made of are scarce, and as such, they are not suitable for large-scale deployment. Alternative catalysts are needed based only on earth-abundant elements, while still providing excellent energy efficiencies.[5] It

has been found that among the earth-abundant elements, cobalt is one of the best alternatives to noble metals[6,7] and catalysts based on cobalt phosphate (CoPi) have demonstrated excellent catalytic performance, both under alkaline and neutral conditions.[8−10] However, as-deposited CoPi layers often do not show good OER performance. Instead, these films require activation by exposure of the film to a high potential for a long time or by repeatedly cycling the applied potential.[11−13] Due to the wide range of employed preparation and activation conditions, the activity of CoPi catalysts reported in the
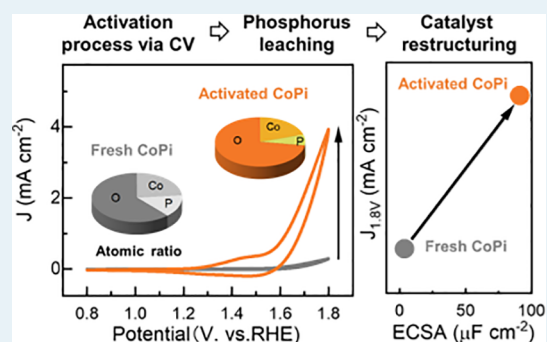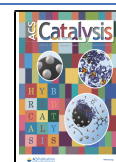
literature is highly inconsistent,[14−16] and much remains unknown about the activation process and the nature of these catalysts under operating conditions.

The activation of CoPi has previously been explained by conversion to amorphous or nanocrystalline cobalt hydroxide.[17] X-ray absorption spectroscopy studies of activated catalysts indicate that this cobalt hydroxide forms nanometer-sized sheets of edge-sharing CoO_6 octahedra, with the intersheet spaces occupied by water molecules and phosphate groups.[18−21] The formation of this layered hydroxide structure is thought to result in the bulk of the film becoming catalytically active.[22] Furthermore, density functional theory calculations indicate that at the surface of these sheets, oxidation of two neighboring Co atoms with pendent oxygen groups to Co^{4+} allows for the direct coupling of these oxygen groups to form O_2, with a simultaneous reduction of the Co^{4+} centers.[23] The phosphate groups in CoPi mediate this process by acting as a flexible support to accommodate morphological changes during oxidation and reduction of the Co centers in the nanosheets, as well as by acting as proton acceptors.[24]

While the characterization of CoPi films before and after activation is reported, limited research has been carried out to gain insight into the (chemical and morphological) changes that CoPi undergo during its activation. Furthermore, the role of the chemical composition of the pristine CoPi film in the whole activation process has not been the subject of investigation so far. In this regard, atomic layer deposition (ALD) offers the opportunity to tune the chemical composition of the electrocatalyst.[25−28] ALD has already been adopted for the deposition of catalysts based on noble metals such as palladium,[29,30] platinum,[31−39] and alloys thereof;[36] transition-metal oxides such as nickel oxide[40−42] and cobalt oxide;[43,44] and various transition-metal phosphates[11] including CoPi.[45] In our previous work, we showed that ALD can be used to prepare smooth, amorphous CoPi films with a tunable chemical composition based on the Co/P atomic ratio.[45] In this work, we further exploit the unique capabilities of ALD in order to study the relationship between chemical and structural changes during activation as well as the influence of the initial film composition on the properties of the activated film. Our results demonstrate that the activation process proceeds in parallel with the progressive leaching of phosphorous and formation of cobalt hydroxide as indicated by X-ray photoelectron spectroscopy (XPS). Analysis of cyclic voltammetry (CV) measurements shows that this change in the chemical composition is directly related to the electrochemical activation of cobalt species and is accompanied by an increase in the OER performance. Subsequently, the effect of the chemical composition of the pristine film (Co/P ratio) on the activation process is studied. The OER activity after activation differs significantly depending on the initial Co/P ratio. By comparing the electrochemical active surface area (ECSA) of these samples, we demonstrate that after activation, the OER activity is directly proportional to the ECSA.

■ RESULTS AND DISCUSSION

Chemical and Morphological Characterization of the As-Deposited Samples. As detailed in the experimental section, CoPi samples were deposited on Si(100) wafers, as well as on fluorine-doped tin oxide (FTO)-coated glass slides, which we will refer to as FTO in the rest of this document. FTO served as a substrate for the electrochemical characterization due to its high conductivity and its poor performance as

an OER catalyst, which allows us to exclude any contribution from the substrate.[45] As the FTO substrate is textured, all quantities reported here have been normalized to the geometric surface area of the sample, rather than the (unknown) exposed surface area, unless noted otherwise. For a discussion on the details of this normalization procedure, we refer to the experimental section. The stoichiometry was varied by adopting a super-cycle approach. These samples have been named CoPi-x, with x corresponding to the Co/P ratios of 1.4, 1.6, 1.7, and 1.9, as determined by XPS. Each sample was deposited using 600 ALD cycles. As a reference, Co_3O_4 samples were also deposited using 600 ALD cycles. Co_3O_4 specifically was chosen as a reference because it is known to not undergo an electrochemical activation process unlike other oxidized cobalt species like CoOOH or $Co(OH)_2$.[46] Cross-sectional scanning electron microscopy (SEM) and spectroscopic ellipsometry measurements revealed that all CoPi films deposited on Si(100) had a thickness of 65 nm, while the thickness of the Co_3O_4 film derived from spectroscopic ellipsometry measurements was 30 nm. A close inspection of the top-view SEM images of pristine FTO and FTO coated with CoPi-1.6 (Figure S1) reveals smoothening of the sharp edges and corners of the FTO crystallites, but no appearance of new crystallites. This also holds for all other CoPi samples. Thus, we conclude that all as-deposited CoPi films, independent of their stoichiometry, conformally coat the FTO substrate. Grazing incidence X-ray diffraction (GIXRD) analysis was used to determine the crystal structure of the samples deposited on FTO, see Figure S2. The FTO substrate is crystalline and exhibits intense diffraction peaks. The GIXRD patterns of the CoPi samples are identical to that of the FTO substrate, indicating that all CoPi samples are amorphous or contain crystallites at a nanoscale insufficient to exhibit diffraction peaks. On the other hand, ALD Co_3O_4 is expected to crystallize in a spinel structure[47] and this is confirmed by the presence of additional diffraction peaks belonging to spinel Co_3O_4.

XPS was used to analyze the chemical composition of CoPi and Co_3O_4 films deposited on FTO. In addition to an adventitious carbon layer, all CoPi samples contained Co, O, and P, while the Co_3O_4 sample contained only Co and O. Figure 1 shows the P 2p, Co 2p, and O 1s XPS spectra of as-deposited CoPi-1.6. For survey spectra and XPS spectra of the other CoPi samples, see Figures S3,S4. The results of this XPS analysis are in agreement with previous reports.[14,48,49] The P
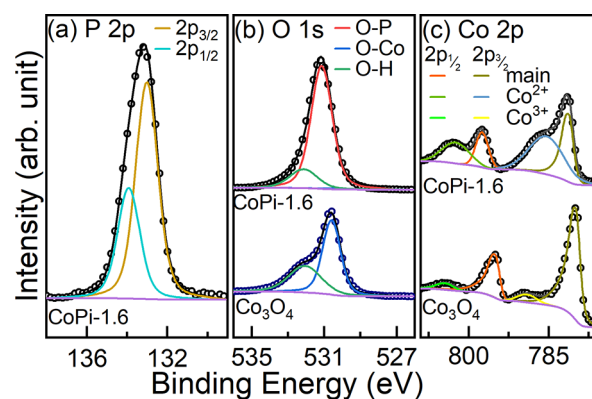

Figure 1. (a) P 2p, (b) O 1s, and (c) Co 2p XPS spectra of as-deposited CoPi-1.6 and Co_3O_4 samples on FTO.

Table 1. Composition and Mass Density of Samples Prepared by ALD on Si(100) Wafers[a]

sample	Co	O	P	H	Co:P	stoichiometry	density
	(10^{15} atoms per cm_{geo}^2)						(g cm^{-3})
CoPi-1.4	124 ± 4	350 ± 20	79 ± 2	6 ± 1	1.57 ± 0.06	$Co_{3.2}P_2O_9$	4.0 ± 0.2
CoPi-1.6	132 ± 4	340 ± 20	75 ± 2	6 ± 1	1.76 ± 0.07	$Co_{3.6}P_2O_{9.2}$	4.1 ± 0.2
CoPi-1.7	142 ± 4	330 ± 20	74 ± 2	7 ± 1	1.92 ± 0.07	$Co_{3.8}P_2O_{9.1}$	4.1 ± 0.2
CoPi-1.9	140 ± 4	33 ± 20	67 ± 2	10 ± 2	2.08 ± 0.09	$Co_{4.2}P_2O_{10.2}$	4.1 ± 0.2
Co_3O_4	138 ± 4	173 ± 8		10 ± 2		$Co_3O_{3.9}$	6.0 ± 0.2

[a]Atomic densities per unit of geometric surface area were measured by RBS and ERD. The stoichiometry of the samples was deduced from these areal densities (excluding H, as it is negligible). Densities were derived from the atomic areal densities determined by RBS and the film thicknesses were determined by spectroscopic ellipsometry (65 nm for the CoPi samples and 30 nm for Co_3O_4).

2p spectrum shown in Figure 1a reveals the presence of a single phosphorous species, associated with the phosphate unit. The O 1s spectrum (Figure 1b) of the CoPi sample is dominated by oxygen species incorporated in phosphate groups. Finally, due to strong spin−orbit coupling, the Co 2p spectrum (Figure 1c) is split into $2p_{3/2}$ and $2p_{1/2}$ contributions. The Co $2p_{3/2}$ region consists of a primary peak at 781.5 eV followed by a broad satellite peak at 785 eV and the same pattern is repeated for the $2p_{1/2}$ region. Furthermore, the energy difference between the primary Co $2p_{3/2}$ and the primary Co $2p_{1/2}$ peaks is 16.0 eV. Both this energy difference and the intense shake-up satellites are characteristic of Co^{2+} species.[50] As the Co 2p region of all CoPi species has nominally the same spectral shape, we conclude that for all Co/P ratios in the range of 1.4 to 1.9, the cobalt atoms are primarily in the 2+ oxidation state.

The spectra recorded for the Co_3O_4 sample are again similar to what has been reported before.[47] The O 1s spectra (Figure 1b) consist of contributions from hydroxyl groups and oxygen atoms bound to cobalt atoms. The Co 2p spectra of the Co_3O_4 sample (Figure 1c) are spin-split, with an energy difference between Co $2p_{3/2}$ and Co $2p_{1/2}$ of 15.0 eV. Furthermore, the intense shake-up satellite observed in the CoPi samples has been replaced with a minor satellite at a binding energy of 790 eV. Together, these results point toward a spectrum dominated by Co^{3+} species.[50] As ALD Co_3O_4 adopts a spinel crystal structure,[47] which contains two Co^{3+} species and one Co^{2+} species per unit cell, a minor contribution from Co^{2+} should be detected in the Co 2p spectra, but it is likely that this contribution is not well resolved as it overlaps with the more intense Co^{3+} contribution.

In order to support the XPS analysis and to obtain the absolute elemental concentration, Rutherford backscattering spectrometry (RBS) and elastic recoil detection (ERD) were employed to verify the elemental composition of CoPi films deposited on Si(100), see Table 1. These analyses confirm that the stoichiometry of the films can be tuned by ALD. Furthermore, they show that these samples have a negligible hydrogen content. Additionally, the densities of all CoPi films, obtained from the atomic loadings per unit of geometric surface area and the film thickness measured by SEM, slightly exceed that of crystalline bulk CoPi (3.8 g cm^{-3}).[51] We assign this to a minor excess of cobalt and oxygen in these films compared to the ideal stoichiometry of $Co_3P_2O_8$.

A systematic difference is observed when comparing the Co/P ratios obtained by RBS and XPS. We assign this difference to the occurrence of an Auger peak of cobalt, which, when using Al Kα radiation, appears at binding energies of ca. 10 eV below that of the Co $2p_{3/2}$ peak.[52] The presence of this Auger signal results in significant uncertainty in the estimation of the

background signal below the Co 2p peaks. The deviations between the Co/P ratios determined by RBS and XPS caused by this Auger peak are structural in nature, with the ratios derived from XPS being ca. 0.2 lower than those derived from RBS in all cases, see Figure S5. As the literature primarily reports XPS data, and generally no correction is made for this Auger peak, in the interest of consistency, we report Co/P ratios as determined by the XPS analysis in the remaining discussion.

Electrochemical Activation of CoPi by Potential Cycling. A detailed study of electrocatalytic water oxidation has been performed in a 0.1 M potassium phosphate (KPi, pH = 8.0) electrolyte solution. As-prepared CoPi and Co_3O_4 films and fresh FTO were taken as working electrodes without further treatment. Cyclic voltammetry (CV) curves were measured for all catalysts and are shown in Figure 2a. In order
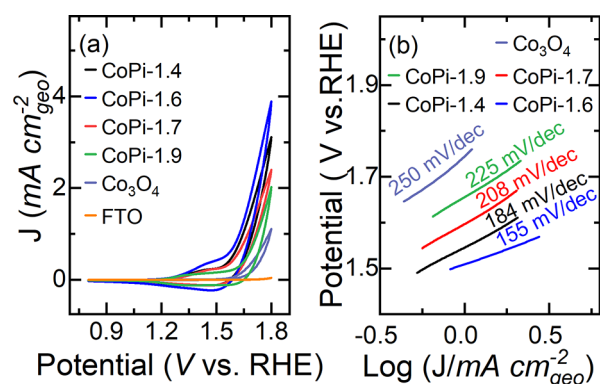

Figure 2. (a) 500th CV sweep of CoPi samples with different initial Co/P ratios as well as Co_3O_4 and pristine FTO. (b) Tafel plots for CoPi films and Co_3O_4 after 500 cycles.

to compare the activities of the CoPi samples in their activated state, they all underwent 500 CV cycles prior to the measurement as shown in Figure 2. As noted before, FTO shows negligible activity toward OER, while the Co_3O_4 film and all CoPi films show significant OER activity. At a potential of 1.8 V versus reversible hydrogen electrode (RHE), CoPi-1.6 displays the highest current density. Tafel analysis was performed to gain insight into the OER kinetics (Figure 2b). The Tafel slope of CoPi-1.6 is comparable to the average Tafel slope (145 mV/dec) reported in the literature for CoPi-based OER catalysts operating under neutral conditions.[14,53,54] We note that this Tafel slope likely contains mass transfer contributions and that they could be improved using gas diffusion electrodes. Nevertheless, for the sake of comparison with the aforementioned literature, we have chosen to limit ourselves to conventional FTO substrates. The lower Tafel

slope of CoPi-1.6 with respect to the other CoPi films suggests a smaller activation energy and a fast reaction rate of the OER. Chronoamperometry shows that after activation, the OER performance of these samples shows acceptable stability, with CoPi-1.6 retaining 86% of its initial activity over 8 h (Figure S6). Thus, CoPi-1.6 turns to be the best sample for OER in 0.1 M KPi, as indicated by a superior Tafel slope, high current density, and good stability. As such, CoPi-1.6 was selected for further investigation of the activation process.

As highlighted in the introduction, CoPi-based electro-catalysts have been found to significantly improve their catalytic performance with an increasing number of CV cycles. To better understand the changes occurring in the film during the activation process, the evolution of the electrochemical properties of Co_3O_4 and CoPi-1.6 was studied in depth as a function of the number of CV sweeps at a scan rate of 10 mV/s, see Figure 3. Co_3O_4 shows a moderate initial current density
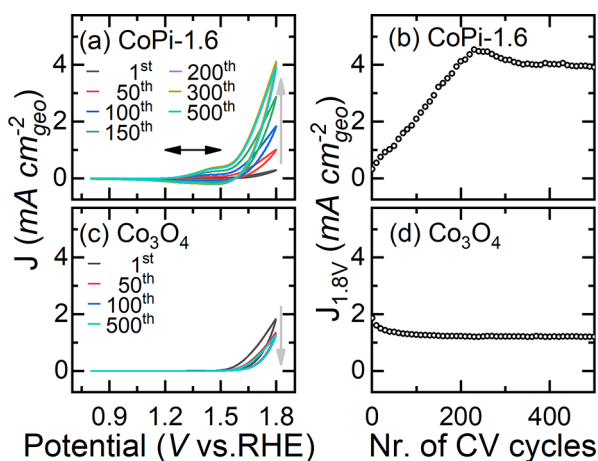

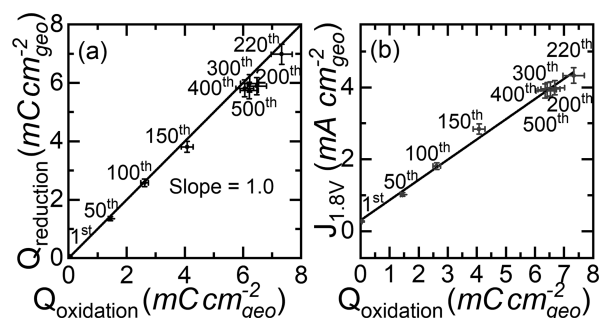**Figure 4.** (a) Relationship between the total amount of charge transferred during noncatalytic oxidation waves ($Q_{oxidation}$) and reduction waves ($Q_{reduction}$) present in the CV sweeps of CoPi-1.6 in a pH 8 KPi buffer. (b) Relationship between the total amount of charge transferred during the noncatalytic oxidative wave and the catalytic current at an applied potential of 1.8 V vs RHE. Symbols represent experimental data points, the line denotes a linear fit to the experimental data, and numbers appearing next to the experimental data points indicate the CV sweeps.

Figure 3. (a) Repeated CV sweeps (scan rate 10 mV s^{-1}) of (a) CoPi-1.6 and (c) Co_3O_4 in a pH 8.0 KPi buffer solution, upon changing the number of CV sweeps. The horizontal arrow indicates the range of a noncatalytic wave. Evolution of the current density of (b) CoPi-1.6 and (d) Co_3O_4 at an applied potential of 1.8 V vs RHE with an increasing number of CV cycles.

during the initial CV cycle, which declines slightly during successive CV cycles. On the other hand, CoPi-1.6 shows an activation process, which leads to an order of magnitude increase in the current density at 1.8 V versus RHE, going from 0.29 mA cm$_{geo}^{-2}$ at the first 1st CV cycle up to 4.5 mA cm$_{geo}^{-2}$ at the 200th CV cycle. Then, the current slightly decreases, reaching 3.9 mA cm$_{geo}^{-2}$ at the 500th cycle. Meanwhile, both oxidative and reductive noncatalytic waves appear between 1.2 and 1.5 V versus RHE. The areas of both noncatalytic waves also increase with CV sweeps.

For activated CoPi catalysts, a close relation between the redox activity (indicated by the total amount of charge transferred during the noncatalytic wave per unit of geometric surface area) and the catalytic activity (indicated by the current density at 1.8 V vs RHE) has been reported previously.[18] The amounts of charge transferred per unit of geometric surface area during the oxidative and reductive noncatalytic waves are linearly correlated, and within experimental error, consistent with a slope of 1.0 (Figure 4a), indicating that the process is reversible. These noncatalytic waves have previously been assigned to the formation of Co^{3+} species,[54,55] and the formation of Co^{3+} in CoPi-1.6 after 500 CV cycles has also

been confirmed by UV−vis spectroscopy (see Figure S7) and XPS (see Figure 5 and associated discussion). However, we did
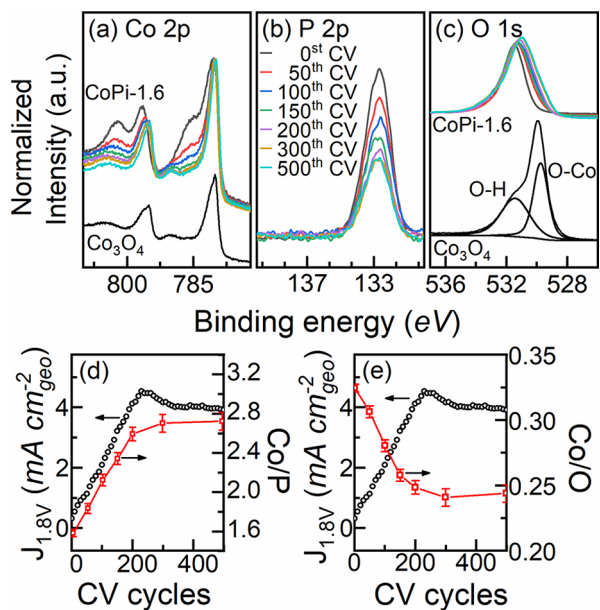

Figure 5. (a−c) Evolution of the Co 2p, P 2p, and O 1s XPS spectra of CoPi-1.6 as a function of the number of CV sweeps. All spectra have been normalized to the height of the Co 2p$_{3/2}$ peak after the corresponding CV sweep. For reference, the surface Co 2p and O 1s XPS spectra of a fresh Co_3O_4 sample have been included and offset vertically. (d) Current density (1.8 eV vs RHE) and Co/P ratio and (e) current density (1.8 eV vs RHE) and Co/O ratio as a function of the number of CV cycles. For clarity, the Co_3O_4 O 1s spectrum has been deconvoluted into contributions from O−H and O−Co species.

not observe the appearance of any new diffraction peaks in GIXRD measurements after activation (Figure S8), indicating that no recrystallization is associated with the formation of these new Co^{3+} species.

As observed by González-Flores et al.,[18] the number of charges transferred during the oxidative wave is linearly correlated to the OER performance (Figure 4b). Co^{3+} species are thought to be the dominant catalytic active centers during the OER.[17,56] After activation, 6.4 mC cm$_{geo}^{-2}$ is transferred

during the noncatalytic wave, which corresponds to 40×10^{15} units of elementary charge per $cm_{geo.}^2$. As this catalytic wave is associated with a 1-electron transfer process, ca. 40×10^{15} Co atoms per cm_{geo}^2 are involved during the noncatalytic wave. From RBS measurements, it follows that CoPi-1.6 contains $(189 \pm 5) \times 10^{15}$ atoms per cm_{geo}^2 (see Table 2 and associated

Table 2. Cobalt and Phosphorous Areal Densities of CoPi-1.6 on FTO before and after OER in a KPi 8.0 Buffer, as Measured by RBS, As Well as the Associated Co/P Ratios[a]

CoPi-1.6	pristine	post-OER	difference
Co (10^{15} atoms per cm_{geo}^2)	203 ± 6	189 ± 5	14 ± 8
P (10^{15} atoms per cm_{geo}^2)	113 ± 3	54 ± 2	59 ± 4
Co/P ratio	1.79 ± 0.07	3.52 ± 0.16	

[a]Note that the density of the pristine samples differs from what is reported in Table 1 due to the texturing of FTO.

discussion). This means that the number of Co atoms that have become redox-active is as high as 22 ± 1% of the total number of Co atoms in the film. We note that this estimation could be lower by up to 50% if we take into consideration also the formation of Co^{4+} during the noncatalytic wave, but this will not substantially affect the following discussion. As previously addressed, the CoPi-1.6 film has a thickness of 65 nm and this film is found to be compact, smooth, and defect-free. If the top 1 nm would be accessible to the electrolyte, 1.5% of the Co atoms in the film would be redox-active. The fact that (i) 22% of the Co atoms were involved during the noncatalytic waves and (ii) the OER performance is proportional to the noncatalytic wave indicate that a significant fraction of the Co atoms in the bulk of the film has become accessible to the electrolyte and is catalytically active. The hypothesis that in CoPi films a significant fraction of the Co atoms below the outer geometric surface of the film is accessible to the electrolyte after activation has been proposed earlier in the literature in order to explain the fact that the activity of CoPi films increases with the film thickness.[22] As such, it can be expected that this activation process may be accompanied by changes in the morphology of the CoPi film that significantly increase the exposed surface area of the film relative to its geometric surface area.

Chemical Changes in CoPi upon Activation. As highlighted in the introduction, activation of the CoPi films is typically accompanied by the partial conversion of cobalt phosphate to layered cobalt oxide or hydroxide. However, it is unknown whether the chemical conversion occurs prior to the activation or develops in parallel with the activation process. In order to shed light on this, CoPi-1.6 films on FTO were subjected to several CV cycles and subsequently their chemical composition was analyzed by XPS. The resulting Co 2p, P 2p, and O 1s XPS spectra obtained after various number of CV cycles are shown in Figure 5a−c. From Figure 5a, we observe that the Co shake-up satellites at 785 and 802 eV (associated with Co^{2+} species) decrease as a function of the number of CV cycles, while the satellite peaks at 790 and 805 eV (associated with Co^{3+} species) increase in intensity. Furthermore, the separation between the Co $2p_{3/2}$ and Co $2p_{1/2}$ main peaks decreases from 16.0 to 15.0 eV, which also suggests a transition from Co^{2+} to Co^{3+}.

Simultaneously with these changes in the Co 2p spectra, the relative intensity of the P 2p spectra decreases (Figure 5b), indicating leaching of phosphate species. The O 1s spectra

shown in Figure 5c show a shift toward a lower binding energy, consistent with an increase in oxygen species bond to cobalt. In addition, there is also an increasing shoulder visible at the high binding energy side, indicating formation of additional hydroxyl groups.[57,58] Taken together, these findings suggest that the activation process is associated with the conversion of CoPi to Co^{3+}-rich cobalt oxide or hydroxide. We find these findings to be universal for all CoPi samples, see Figures S9,S10.

In order to study the relationship between these chemical changes and the electrochemical activity of these films, the Co/P and Co/O ratios obtained from XPS are compared with the current density obtained at 1.8 V versus RHE, see Figure 5d,e. The activation process correlates with a significant increase in the Co/P ratio and a decrease in the Co/O ratio. This is consistent with leaching of phosphorous groups and the incorporation of additional oxygen in the films. When comparing the evolution of the Co/P ratio and the current density, we observe that these two trends are very similar. In both cases, we observe an increase and saturation after ca. 200 CV cycles. The trend for the Co/O ratio is mirrored, that is, it decreases quickly initially, until it also saturates after ca. 200 CV cycles. Referring back to Figure 5a, we also observe that after 200 cycles, changes in the Co 2p spectra are close to saturation, indicating that the change in the stoichiometry and the conversion of Co^{2+} species to Co^{3+} species are correlated. Thus, based on these results, we can conclude that the activation process that leads to an increase in the OER activity of these CoPi films occurs in parallel with the change in their chemical composition.

While these XPS measurements give compelling evidence for conversion of CoPi to cobalt oxide or hydroxide in the near-surface region, they are not representative of the bulk of the film. Therefore, RBS measurements were performed before and after activation of a CoPi-1.6 film on FTO, see Table 2. By comparing the elemental concentration of the as-deposited samples and the samples after 500 CV cycles, we observe a decrease in the phosphorous content of the entire film by approximately 52%, indicating that the loss of phosphorous is not limited to the near-surface region. The fact that XPS can still detect phosphorous suggests that P leaching occurs homogeneously throughout the whole CoPi thickness. Conversely, the amount of cobalt before and after CV cycling differs to within less than 2 standard deviations, indicating that cobalt leaching is within the error of the measurement and thus the change in the film composition can purely be ascribed to the loss of phosphate units.

Effect of pH on the Activation of CoPi. The preliminary conclusion that activation is associated with the loss of phosphate from CoPi suggests that the quantitative leaching of phosphate may lead to a more active catalyst. Therefore, we investigated an alternative activation procedure for CoPi-1.6. A CoPi-1.6 sample was subjected to CV cycling in a 1 M KOH solution (pH = 14) prior to being transferred to a KPi buffer solution (pH = 8.0) for electrochemical characterization. During this alternative activation process, changes in the electrochemical properties of the sample occur much more rapidly than during activation in the KPi buffer, see Figure S11. While activation in KPi took over 200 CV cycles, the activity of CoPi-1.6 in KOH already saturated after 20 cycles.

In the following text, we will refer to the sample activated by 100 CV cycles in 1 M KOH as CoPi-1.6 (act. pH 14), while the sample activated by 500 CV cycles in KPi buffer will be

referred to as CoPi-1.6 (act. pH 8). Figure 6a shows the CV cycles in KPi buffer (pH = 8.0) of CoPi-1.6 (act. pH 8) and
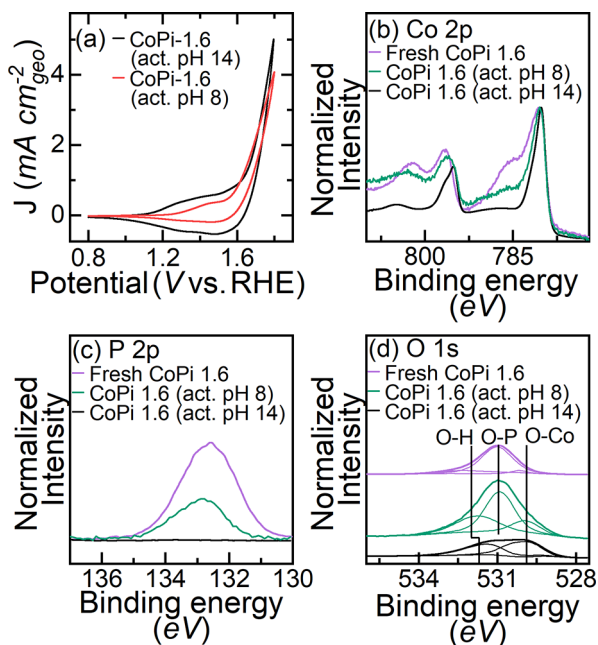

Figure 6. (a) Single CV sweeps CoPi-1.6 activated by 100 CV cycles in a pH 14 KOH solution and CoPi-1.6 activated by 500 CV cycles in a pH 8.0 KPi buffer solution. (b−d) Co 2p, P 2p, and O 1s XPS spectra before and after activation of CoPi-1.6 in a pH 14 KOH solution. Spectra have been normalized to the height of the Co $2p_{3/2}$ peak. The O 1s XPS spectra have been offset for clarity and deconvoluted into contributions from O−H, O−P, and O−Co species.

CoPi-1.6 (act. pH 14): the current density at 1.8 V versus RHE of CoPi-1.6 (act. pH 14) is higher than the current density attained by the film activated at pH 8. In addition to this, the area of the noncatalytic wave of CoPi (act. pH 14) is significantly larger than that of CoPi (act. pH 8). When integrating the noncatalytic wave, we find that 73×10^{15} units of elementary charge are transferred per cm_{geo}^2 during the noncatalytic wave. Since the Co atomic concentration is fixed, we can conclude that $39 \pm 1\%$ of all Co atoms in CoPi-1.6 (act. pH 14) are redox-active, representing a significant increase over CoPi-1.6 (act. pH 8).

XPS measurements were performed on pristine CoPi-1.6, CoPi-1.6 (act. pH 8), and CoPi-1.6 (act. pH 14), see Figure 6b−d for the detailed spectra and Figure S12 for an XPS survey spectrum of CoPi-1.6 (act. pH 14). In order to highlight the changes in the chemical environment, all spectra were normalized to the height of the Co $2p_{3/2}$ peak. Figure 6c shows that at pH 14, the phosphorous loss is complete. A comparison of the Co 2p spectra of CoPi-1.6 (at. pH 8) and CoPi-1.6 (act. pH 14) reveals that the intensity of the Co^{2+} satellite is higher for CoPi-1.6 (act. pH 8) than for CoPi-1.6 (act. pH 14), indicating that some Co^{2+} phosphate remains in CoPi-1.6 (act. pH 8) even after 500 CV cycles. A comparison of the O 1s regions shows a shift of the spectra to lower binding energies when going from pristine CoPi-1.6 to CoPi-1.6 (act. pH 8) and then to CoPi-1.6 (act pH 14). We assign this to progressive loss of the phosphate-related oxygen peak around 531.5 eV and the increase in the cobalt oxide-related O 1s peak at 530.0 eV.

Structural Modifications of CoPi upon Activation. To investigate any structural change associated with the activation process, the activated CoPi-1.6 film (after 500 cycles) was studied by SEM and the corresponding SEM images are shown in Figure 7. Large micrometer-sized cracks appeared on the
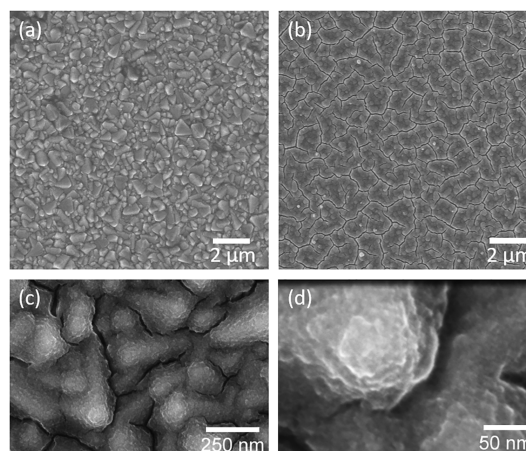

Figure 7. SEM micrographs of CoPi-1.6 (a) as-deposited and (b−d) after 500 CV cycles in a pH 8.0 KPi buffer solution.

surface (Figure 7b), in sharp contrast with the morphology of pristine CoPi-1.6 (Figure 7a), which is crack-free and closely follows the FTO crystallites. We do expect that these cracks are most likely formed due to drying of the film after removal from solution and are therefore not representative of the morphology of the sample during operation.[8,59]

In the uncracked regions, a significant change of microstructure can be observed: the sharp edges from the FTO crystallites present before OER are completely absent after OER and close-packed smoothed features are observed, see Figure 7c. This smoothing of the film suggests that significant restructuring of the initially highly conformal film occurs upon CV cycling. Furthermore, high-magnification SEM reveals that these features contain stacked, poorly ordered platelets (Figure 7d). We tentatively assign the appearance of these platelets to the formation of cobalt oxide or hydroxide nanosheets, which have been identified previously by EXAFS as the dominant phase in activated electrodeposited CoPi catalysts.[18−21]

Influence of the ECSA on the Activation Process. In our previous study,[45] we pointed out to the relationship between the Co/P ratio of the pristine samples and their electrochemical activity. However, as shown here, the composition of CoPi-1.6 changed significantly after activation by 500 CV cycles, and as a matter of fact, Figure S13 shows that there is no universal correlation between the stoichiometry of the layers after activation and their electrochemical activity. In addition to that, as shown previously, the activation process leads to a significant enhancement of the fraction of Co atoms accessible by the electrolyte and for restructuring of the film. As such, while the initial stoichiometry undoubtedly determines the catalytic activity of the samples after activation, the relationship is not direct and there must be an alternative figure of merit that reflects the difference among samples.

The morphological changes that the CoPi films undergo upon their activation can be expected to lead to a significant enhancement of the surface area exposed to the electrolyte for the same amount of geometric surface area immersed in the electrolyte. As such, we characterized the ECSA of the samples

according to their double-layer capacitance (see Figures S14,S15. Note that since the geometric area of the samples is 1 cm^2, in this case, the ECSA also corresponds to the roughness factor). These double-layer capacitances were converted to the corresponding ECSAs using the specific capacitance C_s = 1.7 μF cm$_{ECSA}^{-2}$ obtained from Menezes et al.'s work.[60] When reporting the current density as a function of ECSA (Figure 8), a close relationship between these two
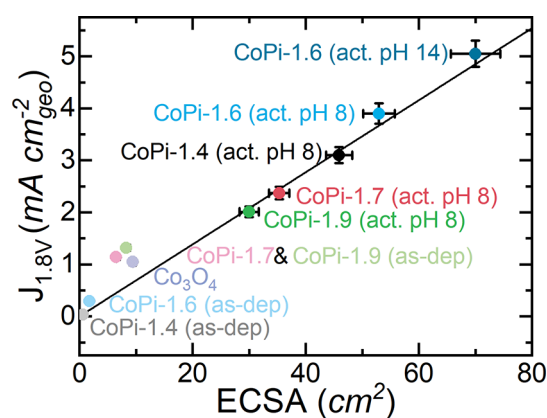

Figure 8. Relationship between the current density at 1.8 V vs RHE in a pH 8.0 KPi buffer solution and the ECSA for samples with different initial Co/P ratios. The symbols represent experimental data points, with error bars indicating the standard error in the current density and ECSA (for some data points, error bars are smaller than the symbols). The line indicates a linear fit to the postactivation experimental data points; for details, see text. For samples marked as-dep, the ECSA was obtained prior to any CV cycling and the current density at 1.8 V vs RHE was obtained from the first CV cycle. Samples marked with act. pH 8 were activated by 500 CV cycles in a pH 8.0 KPi buffer solution prior to the analysis. The sample marked with act. pH 14 was activated by 100 CV cycles in a 1 M KOH solution (pH 14) prior to transfer to the KPi buffer for analysis.

parameters is observed. In particular, all samples prior to activation show an ECSA within one order of magnitude of the geometric surface area of the sample, and a low current density as well. After activation, the current density of all samples increased significantly and at the same time the ECSA increased, thus confirming that the activation process leads to the restructuring of the film that makes a significant part of the bulk of the film accessible to the electrolyte. Furthermore, Figure 8 shows that for the best performing sample after activation, that is, CoPi-1.6, the ECSA increases by a factor 30 upon activation in a pH 8.0 KPi buffer and by a factor of 40 upon activation in a pH 14 KOH solution. Conversely, for the poorest performing sample after activation, CoPi-1.9, the ECSA only increases by a factor 3.6 upon activation in the pH 8.0 KPi buffer.

For all activated samples, including the sample activated in the pH 14 KOH solution, we observe a linear relationship between ECSA and the OER activity, as indicated by the straight-line fit obtained from all activated CoPi samples (note that this fit was forced to yield a current density of 0 mA cm$_{geo}^{-2}$ for an ECSA of 0 cm^2). As such, we can conclude that the activity per unit of ECSA for all activated CoPi samples considered here is roughly equal and that the differences between different samples are governed by differences in the surface area exposed to the electrolyte. While we observe a deviation from this linear behavior for the as-deposited CoPi

samples and the Co$_3$O$_4$ sample (see also Figure S16 for the activity per unit of ECSA), we note that the current density for these samples was derived from the first CV cycle (potentially including some activation), while the ECSA was measured prior to activation. In addition to that, the relationship between C_{dl} and ECSA may change depending on the composition of the solid.[61] The composition of all the activated samples is sufficiently similar to assume a linear correlation between C_{dl} and ECSA, but there is a significant difference in the composition between the as-deposited samples and the activated samples. As such, we cannot say if this deviation represents a difference in the activity per unit of ECSA before and after activation or merely a deviation in the double-layer capacitance per unit of ECSA. Nevertheless, the difference in activity per unit of ECSA of all these samples is far smaller than the typical variation in ECSA found when comparing electrocatalysts prepared using different synthesis methods. In addition to that, Bergmann et al.[46] have shown that the typical variation in activity per unit of ECSA of Co$_3$O$_4$, CoOOH, and Co(OH)$_2$ is relatively small as well. As such, we expect that variations in ECSA typically play a much larger role than variations in the activity per unit of ECSA in determining the activity of cobalt phosphate-, oxide-, and hydroxide-based electrocatalysts.

Nature of the CoPi Activation Process. A comparison of CoPi catalysts with different initial stoichiometries shows that the degree to which their electrochemical activity increases upon activation depends strongly on the initial stoichiometry. Simultaneously, during this activation process, changes in the stoichiometry and ECSA of the films are observed. A higher initial Co/P ratio leads to more extensive leaching of phosphorous from the film, but this does not yield a more active film. Instead, we hypothesize that the activation process involves a restructuring process that simultaneously leads to the loss of phosphate and redistribution of the material across the sample. The fact that the ECSA of these films increases by up to a factor of 40 and over 20% of all Co atoms are redox-active after activation strongly indicates that the activation process proceeds in parallel with CoPi bulk modification. The latter makes the film more accessible to infiltration by the electrolyte. The activity of all CoPi catalysts after this restructuring process is found to be directly correlated to the ECSA. This indicates that the activity per unit of ECSA of the material formed during this restructuring process is quite insensitive to details of the initial stoichiometry or the activation procedure, similar to what was noted by Bergmann et al. for a range of cobalt oxides and hydroxides.[46] However, different pristine chemical compositions are responsible for different ECSAs after activation and the ECSA eventually determines the OER activity of the CoPi film.

As was shown in a recent review by Jiang et al.,[62] electrochemical activation processes are, in general, sensitive to the experimental conditions accompanying the activation process. For several systems, activation at a strongly alkaline pH leads to a more active catalyst. Here, we also observe a strong effect of pH on the activation of CoPi. While activation of CoPi-1.6 at pH 8 leads to an increase in the ECSA by a factor of 30, performing the activation at pH 14 raises this to a factor of 40. We assign this to a more efficient removal of phosphate groups from the bulk of the material and a more complete conversion to cobalt oxide or hydroxide. As the removal of phosphate groups and the restructuring of the layer is likely also dependent on parameters such as temperature, the

potential range and sweep rate of the CV scans, or additives to the buffer solution, we speculate that it might be possible to obtain further enhancement by optimizing the activation conditions. Further work will be needed to elucidate the relationship between activation conditions and the attained ECSA.

CONCLUSIONS

In summary, we have studied the electrocatalytic activity toward OER in neutral media of ALD-prepared CoPi films. The ALD approach allows us to tune the stoichiometries of these CoPi films, which strongly affects the activity of these electrocatalysts after activation. In particular, we find that CoPi films with a Co/P ratio of 1.6 deliver the best OER performance as demonstrated by a high current density (3.95 mA cm$_{geo}^{-2}$ at 1.8 V vs RHE) and a Tafel slope of 155 mV dec^{-1}, which is comparable to other high-performing CoPi-based systems. As films with other Co/P ratios were found to have significantly worse performance, this proves that tuning of the stoichiometry is a valuable tool for obtaining high-performance CoPi-based electrocatalysts.

We find that all ALD-prepared CoPi films undergo an activation process, which is accompanied by chemical composition variation. During catalyst activation by CV, a progressive increase in the OER current density and a noncatalytic wave associated with the conversion of Co^{2+} to Co^{3+} are observed. The number of charges transferred during this noncatalytic wave reveals that during activation, up to 39% of all Co atoms in the film become redox-active. This indicates that a significant part of the bulk of these films becomes accessible to the electrolyte due to the activation process. XPS measurements during the activation process show loss of phosphorous from the film and a progressive conversion from CoPi to cobalt oxide or hydroxide containing primarily Co^{3+} species. This compositional change occurs concurrently with the electrochemical changes highlighted earlier. As similar activation processes have been observed for CoPi-based catalysts deposited hydrothermally, this suggests that for these systems, phosphorous loss is intrinsically linked to the activation process.

We explain these observations by noting that the activation process leads to restructuring of the film, which increases its ECSA up to a factor of 40. The intrinsic activity per unit of ECSA is the same for all activated samples, independent of their preactivation composition. However, differences in the initial stoichiometry lead to a different final ECSA, which is the deciding factor for the overall activity of these films. We argue that this conclusion does not only hold for ALD CoPi films. The phosphate groups in CoPi are a sacrificial component and they can, in principle, be replaced by any other dissolvable species. In fact, in the literature, a wide range of other dissolvable anions has been employed, such as borate[9] or tungstate,[63] and oxidation-induced dissolution has been demonstrated for phosphide- and chalcogenide-based OER catalysts as well.[64] For these films too, we expect a restructuring process to take place and thus the insights described above are likely of general applicability to this whole class of materials.

Finally, we note that the relationship between ECSA and the activity of CoPi films could only be unraveled through a rational control of the film chemical composition. Our results indicate that the ability of ALD to rationally tune the

composition of electrocatalysts allows us to gain insight into their activation mechanism and performance.

EXPERIMENTAL SECTION

Materials and ALD Process. Cobalt phosphate and cobalt oxide thin films were deposited using a home-built plasma-enhanced ALD reactor.[65] The pumping system, consisting of a turbomolecular pump connected to a rotary vane pump, is capable of reaching a base pressure of $< 1 \times 10^{-6}$ mbar. The reactor is equipped with a remote inductively coupled plasma (ICP) source with a power supply operating at 13.56 MHz. During the deposition, the walls of the chamber were heated to 100 °C, while the substrate holder, suitable for fitting a 100 mm-diameter substrate, was heated to 300 °C. Cobaltocene (CoCp$_2$, 98% purity) and Trimethyl phosphate (TMP, (CH$_3$O)$_3$PO, 97% purity), both purchased from Sigma-Aldrich, were selected as precursors for the process. CoCp$_2$ was contained in a stainless steel cylindrical bubbler heated to 80 °C. Argon gas ($> 99.999\%$ purity) was used to carry the CoCp$_2$ vapor from the bubbler to the reactor through a line heated to 100 °C. TMP was vapor-drawn to the chamber; the bubbler containing it was heated to 50 °C and the line to the reactor to 70 °C. For O$_2$ plasma, used as a reactant in the process, O$_2$ gas ($> 99.999\%$ purity) was allowed to flow through the plasma source for 4 s to stabilize the pressure to 8.0×10^{-3} mbar and then the plasma was ignited by providing 100 W of power to the ICP source.

Sample Preparation. Samples with varying stoichiometries were prepared using the approach outlined in our previous work,[45] see Scheme 1. In short, we employed a recipe

Scheme 1. Schematic Illustration of CoPi Film and Co$_3$O$_4$ Film Preparation Process by ALD[a]

[a]The naming scheme for the CoPi samples is used to indicate the Co/P ratio as determined by XPS, for example, in CoPi-1.4, the ratio of cobalt to phosphorous is 1.4.

for the deposition of Co$_3$O$_4$ first developed by Donders et al.[47] and a recipe for the deposition of CoPi developed by Di Palma et al.[66] In order to obtain CoPi films with varying stoichiometries, these two processes were combined in a super-cycle approach. The ALD process for Co$_3$O$_4$ consists of two half-cycles: the first half-cycle of the process is a 2 s CoCp$_2$ precursor dosing step, while the second half-cycle consists of 5 s of O$_2$ plasma exposure. The ALD process for CoPi consists of four half-cycles. The first two half-cycles are the same as the Co$_3$O$_4$ ALD process, the third half-cycle consists of a 0.6 s TMP precursor dosing step, and the last half-cycle is a 2 s O$_2$ plasma exposure step. For the super-cycle processes, each super-cycle consisted of n CoPi deposition cycles followed by one Co$_3$O$_4$ deposition cycle. Samples deposited for n equals to 23, 11, and 5 are referred to as CoPi-1.6, CoPi-1.7, and CoPi-1.9, respectively, with the name indicating the Co/P ratio

obtained in the pristine films as determined by XPS. The CoPi sample deposited using only the CoPi recipe, without Co_3O_4 cycles, is referred to as CoPi-1.4 in order to keep with this naming scheme. The total number of ALD cycles used in each deposition step is 600 to minimize variations in the total cobalt loading. Films for material characterization are deposited on n-type single-crystal Si (100) and FTO on glass.

ALD Film Characterization. The thickness and the dielectric function of the films were monitored during the ALD process by in situ spectroscopic ellipsometry with a J.A. Woollam, Inc. M2000U ellipsometer. Data were recorded within a spectral range between 1.38 and 4.13 eV. A Cauchy dispersion model was utilized to model the CoPi samples and an optical model employing a Gauss, a Tauc−Lorentz, and one Lorentz oscillator was used for Co_3O_4 samples. ERD and RBS measurements were performed using a 2000 keV He^+ beam at a 10° incidence angle with the sample surface, and recoiled atoms were collected at a 25° scattering angle. As the FTO substrate is textured, atomic densities derived from RBS are calculated based on the footprint of the beam rather than the exposed surface area of the sample. X-ray diffraction (XRD) was performed using a PANalytical X'Pert Pro MRD X-ray diffractometer using Cu Kα radiation (λ = 1.540598 Å) in the 2θ range of 20−70° at a scanning rate of 1.5° min^{-1}. Reference XRD patterns were obtained from the International Crystal Structure Database.[67] XPS was performed using a Thermo Scientific K-Alpha system, equipped with a monochromatic Al Kα X-ray source, and the samples were analyzed without further treatment after placement into the UHV system. The surface morphologies of samples were investigated using a field-emission scanning electron microscope (SEM) (Zeiss Sigma, Germany). In order to obtain meaningful SEM results at 1,000,000 times magnification despite drift of the sample and focusing optics, 200 individual images were recorded at 100 ms per image. These images were corrected using the ImageJ plugin TurboReg, which implements a drift correction algorithm developed by Thévenaz et al.[68] Subsequently these images were averaged to obtain a single image with adequate statistics.

OER Measurements. The catalytic activity of the CoPi and Co_3O_4 samples was tested in a 0.1 M (pH 8.0) phosphate buffer solution (HK_2PO_4/H_2KPO_4, KPi) using a single-compartment three-electrode electrochemical cell. Activation in 1 M KOH (pH 14) was performed using the same configuration. CoPi films and Co_3O_4 films on FTO were used as working electrodes. A high-surface Pt mesh was used as a counter electrode, and an Ag/AgCl (saturated) reference electrode was employed. As noted in the main body of the text, the actual area of the samples exposed to the electrolyte is unknown due to the texture of the FTO electrodes. As such, current densities were normalized to the geometric surface area of the substrate immersed into the electrolyte (1 cm^2), which was derived from the lengths of the sides of the triangular section of the substrate in contact with the liquid phase. This introduced an uncertainty of ca. 5% in the immersed surface area, which has been taken into account in determining the uncertainties in the current density and derived quantities. As the use of a Pt counter electrode can lead to deposition of Pt on the sample after repeated potential cycling, XPS measurements were performed after electrochemical analysis. These showed that even after 500 CV cycles, Pt concentrations on the samples were below the detection limits. The electrochemical characterization was carried out using a CompactStat (Ivium)

potentiostat. Electrochemical properties were evaluated by CV, chronoamperometry (i−t), and ECSA. All CV curves were obtained at a scan rate of 10 mV s^{-1} and corrected with 80% iR-compensation. The potential measured was converted to the potential relative to the RHE using the formula: E_{RHE} = $E_{Ag/AgCl}$ + 0.197 V + 0.059 × pH V. Standard errors in current were estimated from the current densities at 1.8 V vs RHE obtained between 400 and 500 CV cycles, after subtraction of a linear background to account for structural loss in activity. Standard errors were found to be less than 1.5% of the absolute current density in all cases. As such, the uncertainty in the current density is effectively determined by the uncertainty in the immersed area of the electrolyte and this has been used to estimate the uncertainties in all quantities derived from CV measurements here. The ECSA for each system was estimated from the electrochemical double-layer capacitance of the catalytic surface (C_{dl}).[61] The electrochemical capacitance was determined by measuring the nonfaradaic capacitive current associated with double-layer charging from the scan-rate dependence of CVs. The CV curves of samples were measured with nonfaradaic potential ranges (0.92 to 1.02 V vs RHE) at various scan rates (5 to 30 mV s^{-1}). Uncertainties in C_{dl} were estimated from the standard error on the slope obtained this way without considering the uncertainty in the integrated currents. This standard error was combined with the uncertainties in the immersed geometric area to estimate the total uncertainty in the double-layer capacitance. As the samples were removed and reimmersed in between CV and C_{dl} measurements, uncertainties in the current density and ECSA were uncorrelated.

■ ASSOCIATED CONTENT

Ⓢ Supporting Information

The Supporting Information is available free of charge at https://pubs.acs.org/doi/10.1021/acscatal.0c04933.

SEM micrographs of bare FTO and as-deposited Co_3O_4, CoPi-1.4, CoPi-1.6, CoPi-1.7, and CoPi-1.9 samples on FTO; GIXRD patterns of FTO and as-deposited Co_3O_4, CoPi-1.4, CoPi-1.6, CoPi-1.7, and CoPi-1.9 samples on FTO; XPS survey spectra of as-deposited Co_3O_4, CoPi-1.4, CoPi-1.6, CoPi-1.7, and CoPi-1.9 samples on FTO; detailed XPS spectra of the Co 2p, P 2p, and O 1s regions of as-deposited Co_3O_4, CoPi-1.4, CoPi-1.6, CoPi-1.7, and CoPi-1.9 samples on FTO; comparison of Co/P ratios in as-deposited CoPi obtained via RBS with the Co/P ratios obtained using XPS; chronoamperometry measurements of CoPi-1.6 at 1.65 V vs RHE; UV−vis spectra of FTO, pristine CoPi-1.6 on FTO, and post-OER CoPi-1.6 on FTO; GIXRD spectra of post-OER CoPi-1.6 on FTO; XPS survey spectra of Co_3O_4, CoPi-1.4, CoPi-1.6, CoPi-1.7, and CoPi-1.9 samples on FTO after activation by 500 CV cycles; detailed XPS spectra of the Co 2p, P 2p, and O 1s regions of Co_3O_4, CoPi-1.4, CoPi-1.6, CoPi-1.7, and CoPi-1.9 samples on FTO after activation by 500 CV cycles; repeated CV sweeps of CoPi-1.6 in 1 M KOH; XPS survey spectrum of CoPi-1.6 activated in pH 14 KOH solution; relationship between Co/P ratio and current density at 1.8 V vs RHE for Co_3O_4, pristine CoPi-1.4, CoPi-1.6, CoPi-1.7, and CoPi-1.9, activated CoPi-1.4, CoPi-1.6, CoPi-1.7, and CoPi-1.9 (activated in pH 8.0 KPi buffer), and CoPi-1.6 activated in 1 M KOH solution; CV curves

of pristine CoPi-1.4, CoPi-1.6, CoPi-1.7, CoPi-1.9, and Co_3O_4 at various scan rates and average variance between the anodic and cathodic currents at 0.97 V vs RHE against the scan rate for these samples; CV curves of CoPi-1.4, CoPi-1.6, CoPi-1.7, CoPi-1.9, and Co_3O_4 after activation at various scan rates and average variance between the anodic and cathodic currents at 0.97 V vs RHE against the scan rate for these samples; and current density at 1.8 V vs RHE per unit of ECSA for Co_3O_4 and all CoPi samples before and after activation (PDF)

■ AUTHOR INFORMATION

Corresponding Authors

Mihalis N. Tsampas − *DIFFER - Dutch Institute For Fundamental Energy Research, 5612 AJ Eindhoven, The Netherlands;* ● orcid.org/0000-0002-4367-4457; Email: m.tsampas@differ.nl

Mariadriana Creatore − *Department of Applied Physics, Eindhoven University of Technology, 5600 MB Eindhoven, The Netherlands;* Email: m.creatore@tue.nl

Authors

Ruoyu Zhang − *Department of Applied Physics, Eindhoven University of Technology, 5600 MB Eindhoven, The Netherlands; DIFFER - Dutch Institute For Fundamental Energy Research, 5612 AJ Eindhoven, The Netherlands*

Gerben van Straaten − *Department of Applied Physics, Eindhoven University of Technology, 5600 MB Eindhoven, The Netherlands;* ● orcid.org/0000-0002-6004-5740

Valerio di Palma − *Department of Applied Physics, Eindhoven University of Technology, 5600 MB Eindhoven, The Netherlands*

Georgios Zafeiropoulos − *DIFFER - Dutch Institute For Fundamental Energy Research, 5612 AJ Eindhoven, The Netherlands*

Mauritius C.M. van de Sanden − *Department of Applied Physics, Eindhoven University of Technology, 5600 MB Eindhoven, The Netherlands; DIFFER - Dutch Institute For Fundamental Energy Research, 5612 AJ Eindhoven, The Netherlands;* ● orcid.org/0000-0002-4119-9971

Wilhelmus M.M. Kessels − *Department of Applied Physics, Eindhoven University of Technology, 5600 MB Eindhoven, The Netherlands;* ● orcid.org/0000-0002-7630-8226

Complete contact information is available at:
https://pubs.acs.org/10.1021/acscatal.0c04933

Author Contributions

§R.Z. and G.V.S. have contributed equally and possess the first authorship of this article. M.C. and M.N.T. conceived the idea of this study and supervised the research. R.Z. synthesized the ALD electrocatalysts with the assistance of V.d.P. R.Z. collected and analyzed the XRD, XPS, RBS, UV−vis, SEM, and electrochemical data with assistance from G.v.S. and G.Z. G.v.S. drafted the manuscript with assistance from R.Z. W.M.M.K. and M.C.M.v.d.S. provided suggestions on data interpretation and manuscript refinement. M.C., M.N.T, W.M.M.K., and M.C.M.v.d.S. secured the funding for the project. All authors discussed the results and commented on the manuscript.

Notes

The authors declare no competing financial interest.

■ ACKNOWLEDGMENTS

■ REFERENCES

(1) Cai, Z. S.; Shi, Y.; Bao, S. S.; Shen, Y.; Xia, X. H.; Zheng, L. M. Bioinspired Engineering of Cobalt-Phosphonate Nanosheets for Robust Hydrogen Evolution Reaction. *ACS Catal.* **2018**, *8*, 3895−3902.

(2) Niakolas, D. K.; Daletou, M.; Neophytides, S. G.; Vayenas, C. G. Fuel Cells Are a Commercially Viable Alternative for the Production of "Clean" Energy. *Ambio* **2016**, *45*, 32−37.

(3) Kato, T.; Kubota, M.; Kobayashi, N.; Suzuoki, Y. Effective Utilization of By-Product Oxygen from Electrolysis Hydrogen Production. In *Energy; Elsevier Ltd* **2005**, *30*, 2580−2595.

(4) Buttler, A.; Spliethoff, H. Current Status of Water Electrolysis for Energy Storage, Grid Balancing and Sector Coupling via Power-to-Gas and Power-to-Liquids: A Review. *Renew. Sustain. Energy Rev.* **2018**, *82*, 2440−2454.

(5) Xu, W.; Wang, H. Earth-Abundant Amorphous Catalysts for Electrolysis of Water. *Cuihua Xuebao/Chinese J. Catal.* **2017**, *38*, 991−1005.

(6) Zhang, W.; Cui, L.; Liu, J. Recent Advances in Cobalt-Based Electrocatalysts for Hydrogen and Oxygen Evolution Reactions. *J. Alloys Compd. Elsevier Ltd April* **2020**, *821*, No. 153542.

(7) Xu, J.; Murphy, S.; Xiong, D.; Cai, R.; Wei, X. K.; Heggen, M.; Barborini, E.; Vinati, S.; Dunin-Borkowski, R. E.; Palmer, R. E.; Liu, L. Cluster Beam Deposition of Ultrafine Cobalt and Ruthenium Clusters for Efficient and Stable Oxygen Evolution Reaction. *ACS Appl. Energy Mater.* **2018**, *1*, 3013−3018.

(8) Kanan, M. W.; Nocera, D. G. In Situ Formation of an Oxygen-Evolving Catalyst in Neutral Water Containing Phosphate and Co^{2+}. *Science (80-.)* **2008**, *321*, 1072−1075.

(9) Esswein, A. J.; Surendranath, Y.; Reece, S. Y.; Nocera, D. G. Highly Active Cobalt Phosphate and Borate Based Oxygen Evolving Catalysts Operating in Neutral and Natural Waters. *Energy Environ. Sci.* **2011**, *4*, 499−504.

(10) Surendranath, Y.; Dincǎ, M.; Nocera, D. G. Electrolyte-Dependent Electrosynthesis and Activity of Cobalt-Based Water Oxidation Catalysts. *J. Am. Chem. Soc.* **2009**, *131*, 2615−2620.

(11) Rongé, J.; Dobbelaere, T.; Henderick, L.; Minjauw, M. M.; Sree, S. P.; Dendooven, J.; Martens, J. A.; Detavernier, C. Bifunctional Earth-Abundant Phosphate/Phosphide Catalysts Prepared: Via Atomic Layer Deposition for Electrocatalytic Water Splitting. *Nanoscale Adv.* **2019**, *1*, 4166−4172.

(12) Costentin, C.; Porter, T. R.; Savéant, J. M. Conduction and Reactivity in Heterogeneous-Molecular Catalysis: New Insights in Water Oxidation Catalysis by Phosphate Cobalt Oxide Films. *J. Am. Chem. Soc.* **2016**, *138*, 5615−5622.

(13) Sonwalkar, H. S.; Haram, S. K. Kinetic Analysis of the Oxygen Evolution Reaction (OER) Performed with a Cobalt-Phosphate Electrocatalyst. *ChemistrySelect* **2017**, *2*, 3323−3328.

(14) Xie, L.; Zhang, R.; Cui, L.; Liu, D.; Hao, S.; Ma, Y.; Du, G.; Asiri, A. M.; Sun, X. High-Performance Electrolytic Oxygen Evolution in Neutral Media Catalyzed by a Cobalt Phosphate Nanoarray. *Angew Chemie - Int Ed.* **2017**, *56*, 1064−1068.

(15) Pramanik, M.; Li, C.; Imura, M.; Malgras, V.; Kang, Y. M.; Yamauchi, Y. Ordered Mesoporous Cobalt Phosphate with Crystal-

lized Walls toward Highly Active Water Oxidation Electrocatalysts. *Small* **2016**, *12*, 1709−1715.

(16) Vasileff, A.; Chen, S.; Qiao, S. Z. Three Dimensional Nitrogen-Doped Graphene Hydrogels with: In Situ Deposited Cobalt Phosphate Nanoclusters for Efficient Oxygen Evolution in a Neutral Electrolyte. *Nanoscale Horiz.* **2016**, *1*, 41−44.

(17) Gerken, J. B.; McAlpin, J. G.; Chen, J. Y. C.; Rigsby, M. L.; Casey, W. H.; Britt, R. D.; Stahl, S. S. Electrochemical Water Oxidation with Cobalt-Based Electrocatalysts from pH 0-14: The Thermodynamic Basis for Catalyst Structure, Stability, and Activity. *J. Am. Chem. Soc.* **2011**, *133*, 14431−14442.

(18) González-Flores, D.; Sánchez, I.; Zaharieva, I.; Klingan, K.; Heidkamp, J.; Chernev, P.; Menezes, P. W.; Driess, M.; Dau, H.; Montero, M. L. Heterogeneous Water Oxidation: Surface Activity versus Amorphization Activation in Cobalt Phosphate Catalysts. *Angew. Chemie - Int Ed.* **2015**, *54*, 2472−2476.

(19) Yano, J.; Yachandra, V. K.; Kanan, M. W.; Surendranath, Y.; Dinca, M.; Nocera, D. G. An Artificial Water-Oxidizing Co Electro-Catalyst: Structure and Mechanism by in Situ x-Ray Absorption Spectroscopy. *Adv. Top. Sci. Technol* **2013**, 266−268.

(20) Farrow, C. L.; Bediako, D. K.; Surendranath, Y.; Nocera, D. G.; Billinge, S. J. L. Intermediate-Range Structure of Self-Assembled Cobalt-Based Oxygen-Evolving Catalyst. *J. Am. Chem. Soc.* **2013**, *135*, 6403−6406.

(21) Kanan, M. W.; Yano, J.; Surendranath, Y.; Dincă, M.; Yachandra, V. K.; Nocera, D. G. Structure and Valency of a Cobalt-Phosphate Water Oxidation Catalyst Determined by in Situ X-Ray Spectroscopy. *J. Am. Chem. Soc.* **2010**, *132*, 13692−13701.

(22) Klingan, K.; Ringleb, F.; Zaharieva, I.; Heidkamp, J.; Chernev, P.; Gonzalez-Flores, D.; Risch, M.; Fischer, A.; Dau, H. Water Oxidation by Amorphous Cobalt-Based Oxides: Volume Activity and Proton Transfer to Electrolyte Bases. *ChemSusChem* **2014**, *7*, 1301−1310.

(23) Wang, L. P.; Van Voorhis, T. Direct-Coupling O_2 Bond Forming a Pathway in Cobalt Oxide Water Oxidation Catalysts. *J. Phys. Chem. Lett.* **2011**, *2*, 2200−2204.

(24) Shao, Y.; Xiao, X.; Zhu, Y. P.; Ma, T. Y. Single-Crystal Cobalt Phosphate Nanosheets for Biomimetic Oxygen Evolution in Neutral Electrolytes. *Angew. Chemie - Int Ed.* **2019**, *58*, 14599−14604.

(25) Van Bui, H.; Grillo, F.; Van Ommen, J. R. Atomic and Molecular Layer Deposition: Off the Beaten Track. *Chem. Commun* **2017**, *53*, 45−71.

(26) Cao, K.; Cai, J.; Liu, X.; Chen, R. Review Article: Catalysts Design and Synthesis via Selective Atomic Layer Deposition. *J. Vac. Sci. Technol. A Vacuum, Surfaces, Film* **2018**, *36*, No. 010801.

(27) Oneill, B. J.; Jackson, D. H. K.; Lee, J.; Canlas, C.; Stair, P. C.; Marshall, C. L.; Elam, J. W.; Kuech, T. F.; Dumesic, J. A.; Huber, G. W. Catalyst Design with Atomic Layer Deposition. *ACS Catal.* **2015**, *5*, 1804−1825.

(28) Lu, J.; Elam, J. W.; Stair, P. C. Atomic Layer Deposition - Sequential Self-Limiting Surface Reactions for Advanced Catalyst "Bottom-up" Synthesis. *Surf. Sci. Rep.. Elsevier B.V.* **2016**, *71*, 410−472.

(29) Weber, M.; Collot, P.; El Gaddari, H.; Tingry, S.; Bechelany, M.; Holade, Y. Enhanced Catalytic Glycerol Oxidation Activity Enabled by Activated-Carbon-Supported Palladium Catalysts Prepared through Atomic Layer Deposition. *ChemElectroChem* **2018**, *5*, 743−747.

(30) Weber, M. J.; MacKus, A. J. M.; Verheijen, M. A.; Longo, V.; Bol, A. A.; Kessels, W. M. M. Atomic Layer Deposition of High-Purity Palladium Films from Pd(Hfac)$_2$ and H_2 and O_2 Plasmas. *J. Phys. Chem. C* **2014**, *118*, 8702−8711.

(31) Kessels, W. M. M.; Knoops, H. C. M.; Dielissen, S. A. F.; MacKus, A. J. M.; Van De Sanden, M. C. M. Surface Reactions during Atomic Layer Deposition of Pt Derived from Gas Phase Infrared Spectroscopy. *Appl. Phys. Lett.* **2009**, *95*, No. 013114.

(32) Liu, C.; Wang, C. C.; Kei, C. C.; Hsueh, Y. C.; Perng, T. P. Atomic Layer Deposition of Platinum Nanoparticles on Carbon Nanotubes for Application in Proton-Exchange Membrane Fuel Cells. *Small* **2009**, *5*, 1535−1538.

(33) King, J. S.; Wittstock, A.; Biener, J.; Kucheyev, S. O.; Wang, Y. M.; Baumann, T. F.; Giri, S. K.; Hamza, A. V.; Baeumer, M.; Bent, S. F. Ultralow Loading Pt Nanocatalysts Prepared by Atomic Layer Deposition on Carbon Aerogels. *Nano Lett.* **2008**, *8*, 2405−2409.

(34) Jiang, X.; Huang, H.; Prinz, F. B.; Bent, S. F. Application of Atomic Layer Deposition of Platinum to Solid Oxide Fuel Cells. *Chem. Mater.* **2008**, *20*, 3897−3905.

(35) Christensen, S. T.; Feng, H.; Libera, J. L.; Guo, N.; Miller, J. T.; Stair, P. C.; Elam, J. W. Supported Ru-Pt Bimetallic Nanoparticle Catalysts Prepared by Atomic Layer Deposition. *Nano Lett.* **2010**, *10*, 3047−3051.

(36) Jiang, X.; Gür, T. M.; Prinz, F. B.; Bent, S. F. Atomic Layer Deposition (ALD) Co-Deposited Pt-Ru Binary and Pt Skin Catalysts for Concentrated Methanol Oxidation. *Chem. Mater.* **2010**, *22*, 3024−3032.

(37) Vos, M. F. J.; Van Straaten, G.; Kessels, W. M. M. E.; Mackus, A. J. M. Atomic Layer Deposition of Cobalt Using H_2-, N_2-, and NH_3-Based Plasmas: On the Role of the Co-Reactant. *J. Phys. Chem. C* **2018**, *122*, 22519.

(38) Mackus, A. J. M.; Verheijen, M. A.; Leick, N.; Bol, A. A.; Kessels, W. M. M. Influence of Oxygen Exposure on the Nucleation of Platinum Atomic Layer Deposition: Consequences for Film Growth, Nanopatterning, and Nanoparticle Synthesis. *Chem. Mater.* **2013**, *25*, 1905−1911.

(39) Mackus, A. J. M.; Leick, N.; Baker, L.; Kessels, W. M. M. Catalytic Combustion and Dehydrogenation Reactions during Atomic Layer Deposition of Platinum. *Chem. Mater.* **2012**, *24*, 1752−1761.

(40) Koushik, D.; Jošt, M.; Dučinskas, A.; Burgess, C.; Zardetto, V.; Weijtens, C.; Verheijen, M. A.; Kessels, W. M. M.; Albrecht, S.; Creatore, M. Plasma-Assisted Atomic Layer Deposition of Nickel Oxide as Hole Transport Layer for Hybrid Perovskite Solar Cells. *J. Mater. Chem. C* **2019**, *7*, 12532−12543.

(41) Zeng, J.; Xu, X.; Parameshwaran, V.; Baker, J.; Bent, S.; Wong, H. S. P.; Clemens, B. Photoelectrochemical Water Oxidation by GaAs Nanowire Arrays Protected with Atomic Layer Deposited NiO$_x$ Electrocatalysts. *J. Electron. Mater Springer New York LLC* **2018**, *47*, 932−937.

(42) Zhong, M.; Hisatomi, T.; Minegishi, T.; Nishiyama, H.; Katayama, M.; Yamada, T.; Domen, K. Bulky Crystalline BiVO$_4$ Thin Films for Efficient Solar Water Splitting. *J. Mater. Chem. A* **2016**, *4*, 9858−9864.

(43) Huang, B.; Yang, W.; Wen, Y.; Shan, B.; Chen, R. Co$_3$O$_4$-Modified TiO2 Nanotube Arrays via Atomic Layer Deposition for Improved Visible-Light Photoelectrochemical Performance. *ACS Appl. Mater. Interfaces* **2014**, *7*, 422−431.

(44) Du, C.; Wang, J.; Liu, X.; Yang, J.; Cao, K.; Wen, Y.; Chen, R.; Shan, B. Ultrathin CoOx-Modified Hematite with Low Onset Potential for Solar Water Oxidation. *Phys. Chem. Chem. Phys.* **2017**, *19*, 14178−14184.

(45) Di Palma, V.; Zafeiropoulos, G.; Goldsweer, T.; Kessels, W. M. M.; van de Sanden, M. C. M.; Creatore, M.; Tsampas, M. N. Atomic Layer Deposition of Cobalt Phosphate Thin Films for the Oxygen Evolution Reaction. *Electrochem. Commun* **2019**, *98*, 73−77.

(46) Bergmann, A.; Jones, T. E.; Martinez Moreno, E.; Teschner, D.; Chernev, P.; Gliech, M.; Reier, T.; Dau, H.; Strasser, P. Unified Structural Motifs of the Catalytically Active State of Co(Oxyhydr)-Oxides during the Electrochemical Oxygen Evolution Reaction. *Nat. Catal.* **2018**, *1*, 711−719.

(47) Donders, M. E.; Knoops, H. C. M.; Van, M. C. M.; Kessels, W. M. M.; Notten, P. H. L. Remote Plasma Atomic Layer Deposition of Co$_3$O$_4$ Thin Films. *J. Electrochem. Soc.* **2011**, *158*, G92.

(48) Wang, X.; Ma, W.; Ding, C.; Xu, Z.; Wang, H.; Zong, X.; Li, C. Amorphous Multi-Elements Electrocatalysts with Tunable Bifunctionality toward Overall Water Splitting. *ACS Catal.* **2018**, *8*, 9926−9935.

(49) Li, Y.; Zhao, Y.; Zhang, Z. A. Porous Graphene/Cobalt Phosphate Composite as an Efficient Oxygen Evolving Catalyst. *Electrochem. Commun.* **2014**, *48*, 35−39.

(50) Oku, M.; Hirokawa, K. X-Ray Photoelectron Spectroscopy of Co$_3$O$_4$, Fe$_3$O$_4$, Mn$_3$O$_4$, and Related Compounds. *J. Electron Spectros. Relat. Phenomena* **1976**, *8*, 475−481.

(51) Anderson, J. B.; Kostiner, E.; Miller, M. C.; Rea, J. R. The Crystal Structure of Cobalt Orthophosphate Co$_3$(PO$_4$)$_2$. *J. Solid State Chem* **1975**, *14*, 372−377.

(52) Farr, N. G.; Griesser, H. J. XPS Excitation Dependence of Measured Cobalt 2p$_{3/2}$ Peak Intensity Due to Auger Peak Interference. *J. Electron Spectros. Relat. Phenomena* **1989**, *49*, 293−302.

(53) Saha, J.; Verma, S.; Ball, R.; Subramaniam, C.; Murugavel, R. Compositional Control as the Key for Achieving Highly Efficient OER Electrocatalysis with Cobalt Phosphates Decorated Nanocarbon Florets. *Small* **2020**, *16*, No. 1903334.

(54) Wan, H.; Ma, R.; Liu, X.; Pan, J.; Wang, H.; Liang, S.; Qiu, G.; Sasaki, T. Rare Cobalt-Based Phosphate Nanoribbons with Unique 5-Coordination for Electrocatalytic Water Oxidation. *ACS Energy Lett.* **2018**, *3*, 1254−1260.

(55) McAlpin, J. G.; Surendranath, Y.; Dincă, M.; Stich, T. A.; Stoian, S. A.; Casey, W. H.; Nocera, D. G.; Britt, R. D. Evidence for Co(IV) Species Produced during Water Oxidation at Neutral PH. *J. Am. Chem. Soc.* **2010**, *132*, 6882−6883.

(56) Smith, R. D. L.; Pasquini, C.; Loos, S.; Chernev, P.; Klingan, K.; Kubella, P.; Mohammadi, M. R.; Gonzalez-Flores, D.; Dau, H. Spectroscopic Identification of Active Sites for the Oxygen Evolution Reaction on Iron-Cobalt Oxides. *Nat. Commun.* **2017**, *8*, 1−8.

(57) Zhu, M.; Han, M.; Zhu, C.; Hu, L.; Huang, H.; Liu, Y.; Kang, Z. Strong Coupling Effect at the Interface of Cobalt Phosphate-Carbon Dots Boost Photocatalytic Water Splitting. *J. Colloid Interface Sci.* **2018**, *530*, 256−263.

(58) Lu, W. X.; Wang, B.; Chen, W. J.; Xie, J. L.; Huang, Z. Q.; Jin, W.; Song, J. L. Nanosheet-like Co$_3$(OH)$_2$(HPO$_4$)$_2$ as a Highly Efficient and Stable Electrocatalyst for Oxygen Evolution Reaction. *ACS Sustainable Chem. Eng.* **2019**, *7*, 3083−3091.

(59) Cobo, S.; Heidkamp, J.; Jacques, P. A.; Fize, J.; Fourmond, V.; Guetaz, L.; Jousselme, B.; Ivanova, V.; Dau, H.; Palacin, S.; Fontecave, M.; Artero, V. A Janus Cobalt-Based Catalytic Material for Electro-Splitting of Water. *Nat. Mater.* **2012**, *11*, 802−807.

(60) Menezes, P. W.; Panda, C.; Walter, C.; Schwarze, M.; Driess, M. A. Cobalt-Based Amorphous Bifunctional Electrocatalysts for Water-Splitting Evolved from a Single-Source Lazulite Cobalt Phosphate. *Adv. Funct. Mater.* **2019**, *29*, No. 1808632.

(61) McCrory, C. C. L.; Jung, S.; Peters, J. C.; Jaramillo, T. F. Benchmarking Heterogeneous Electrocatalysts for the Oxygen Evolution Reaction. *J. Am. Chem. Soc.* **2013**, *135*, 16977−16987.

(62) Jiang, H.; He, Q.; Zhang, Y.; Song, L. Structural Self-Reconstruction of Catalysts in Electrocatalysis. *Acc. Chem. Res.* **2018**, *51*, 2968−2977.

(63) Tian, T.; Jiang, J.; Ai, L. In Situ Electrochemically Generated Composite-Type CoO$_x$/WO$_x$ in Self-Activated Cobalt Tungstate Nanostructures: Implication for Highly Enhanced Electrocatalytic Oxygen Evolution. *Electrochim. Acta* **2017**, *224*, 551−560.

(64) Li, W.; Xiong, D.; Gao, X.; Liu, L. The Oxygen Evolution Reaction Enabled by Transition Metal Phosphide and Chalcogenide Pre-Catalysts with Dynamic Changes. *Chem. Commun.* **2019**, *55*, 8744−8763.

(65) Heil, S. B. S.; Langereis, E.; Roozeboom, F.; van de Sanden, M. C. M.; Kessels, W. M. M. Low-Temperature Deposition of TiN by Plasma-Assisted Atomic Layer Deposition. *J. Electrochem. Soc.* **2006**, *153*, G956.

(66) Di Palma, V.; Knoops, H. C. M.; Kessels, W. M. M. E.; Creatore, M. Atomic Layer Deposition of Cobalt Phosphate from Cobaltocene, Trimethylphosphate, and O$_2$ Plasma. *J. Vac. Sci. Technol., A* **2020**, *38*, No. 022416.

(67) Bergerhoff, G.; Brown, I. D.. In *Crystallographic Databases*; Allen, F. H., Bergerhoff, G., Sievers, R., Eds.; International Union of Crystallography: Chester, 1987.

(68) Thévenaz, P.; Ruttimann, U. E.; Unser, M. A. Pyramid Approach to Subpixel Registration Based on Intensity. *IEEE Trans. Image Process.* **1998**, *7*, 27−41.